Hidden Mn magnetic-moment disorder and its influence on the physical properties of medium-entropy NiCoMn solid solution alloys

Sai Mu,[1,*] J. Yin,[2] G. D. Samolyuk,[1] S. Wimmer,[3] Z. Pei,[1] M. Eisenbach,[2] S. Mankovsky,[3] H. Ebert,[3] and G. M. Stocks[1,†]
[1]*Materials Science and Technology Division, Oak Ridge National Laboratory, Oak Ridge, Tennessee 37831, USA*
[2]*National Center for Computational Sciences, Oak Ridge National Laboratory, Oak Ridge, Tennessee 37831, USA*
[3]*Department of Chemistry, Ludwig-Maximilians-Universität, D-81377 Munchen, Germany*

(Received 6 November 2018; published 22 January 2019)

The *ab initio* Korringa-Kohn-Rostoker method combined with the coherent potential approximation (CPA) was employed to investigate the electronic, magnetic, and transport properties of medium-entropy face-centered-cubic (fcc) NiCoMn solid solution alloys. By comparing the CPA electronic structure with that from supercell calculations, we uncovered an unconventional CPA ground state, which correctly distinguishes two equally populated Mn CPA components—with large spin moments but opposite orientations. Using the spin spiral calculations, we further demonstrated that this ground state is most energetically favorable in the presence of spin noncollinearity, and no significant longitudinal spin fluctuation is observed, justifying the applicability of the Heisenberg model. The finite-temperature magnetism was further studied using different approximations based on the Heisenberg model, and we found the Mn moments to be fully disordered at low temperature due to a small net effective Weiss field on Mn. In addition, the magnetic effect on the electron scattering at finite temperatures was evaluated and compared with other scattering mechanisms. Since the magnetization-induced electron scattering is almost saturated in the ground state, (full) spin disorder only yields a small addition to the resistivity, whereas the thermal displacements increase it modestly. Finally, we elucidate the role of hydrostatic pressure on the magnetic and transport properties. These findings reflect the importance of the magnetic signatures on the physical properties of alloys, and they provide a window into magnetism-controlled electronic structure and energy dissipation.

DOI: 10.1103/PhysRevMaterials.3.014411

I. INTRODUCTION

In a general N-component concentrated solid-solution alloy (CSA), the configurational entropy is maximal at equiatomic concentration and increases with the number of alloying elements N. When $N \geqslant 5$, Yeh *et al.* [1] argued that the contribution from the configurational entropy to the Gibbs free energy may be dominant, thereby facilitating the formation of highly stable, single-phase disordered solid solution alloys, of which high entropy alloys (HEAs) are exemplars [2]. Following the synthesis of the first HEA (NiFeCoCrMn) by Cantor *et al.* [3], Wu *et al.* [4] demonstrated that by taking combinations of this alloy's 3*d* transition-metal elements, supplemented by Pd, it is possible to obtain a series of two-, three-, four-, and five-component equiatomic alloys (NiCo, NiFe, NiPd, NiFeCo, NiCoCr, NiCoMn, NiCoCrMn, NiFeCoCr, NiFeCoMn, NiFeCoCrMn, and NiFeCoCrPd) that all crystallize as a single-phase face-centered-cubic (fcc) solid solution alloy. Hereafter, this set of Ni-based fcc alloys will be referred to as Cantor-Wu alloys. Since the discovery of HEAs, many exceptional and unusual properties—mechanical [5,6], radiation response [7,8], transport [9–11], and magnetic properties [10,12]—have been reported for alloys having a variety of crystal structures, including fcc [4], body-centered-cubic (bcc) [13], and hexagonal-closed-packed (hcp) [14].

In disordered alloys composed of midperiod 3*d* transition-metal elements, magnetism is well known to play an important role in determining their properties. First, magnetic entropy makes a substantial contribution to the Gibbs free energy, thereby affecting thermodynamic phase-stability-related phenomena, such as order-disorder [15], and structural phase transitions, e.g., fcc-hcp transitions that are controlled by the stacking fault energies [16,17]. In addition, magnetism can have a large impact on other properties, including mechanical properties [18,19], electronic [20] and thermal transport [9,21], and thermal expansion, such as the Invar effect in iron-nickel alloys [22], and it also holds promise for functional applications, such as giant spin-orbit torque [23]. However, unlike mechanical properties that have been explored extensively, studies of magnetic properties and the influence of magnetism on other derived properties of CSAs and HEAs remain scarce and deserve further investigation.

In this work, we study the magnetic properties of the medium-entropy CSA NiCoMn, which can be regarded as a prototype of many Mn-containing Cantor-Wu alloys (NiCoMn, NiFeCoMn, NiCoCrMn, and NiFeCoCrMn), several of which exhibit complex magnetic properties, such as a spin-glass state [12], frustrated Mn moments [18], longitudinal spin fluctuations (LSF) [19], and low critical temperature (T_c) [10]. Interestingly, alloying NiCoMn with Fe to form a NiFeCoMn solid solution gives unremarkable mechanical

*sai.mu1986321@gmail.com
†stocksgm@ornl.gov

properties [24,25], while supplementing NiCoMn with Cr yields an excellent combination of strength and ductility [5]. In addition, it has been suggested that the occurrence of frustrated Mn moments [18] can eliminate the fcc-hcp energy difference, and thereby directly impact the fcc-hcp phase transition and resulting mechanical properties. Therefore, a deep understanding of magnetism in the NiCoMn alloy is a prerequisite for understanding other properties of Mn-containing Cantor-Wu alloys.

Interestingly, the two most prevalent *ab initio* theories of disordered alloys—the supercell method [26] and the coherent potential approximation (CPA) [27]—contradict each other regarding the magnetic ground state of some Mn-containing Cantor-Wu alloys. On the one hand, supercell calculations found two (approximately equally populated) groups of Mn atoms, each with sizable local moments but having opposite spin orientations [18,20]. On the other hand, conventional single-site CPA calculations yield only *one* type of Mn atom, all having low spin moments (hereafter called the one-Mn model). Interestingly, this lattice CPA approach has been employed to study the stacking fault energies [28], magnetic transition temperatures [29], longitudinal spin fluctuations, and the impact of magnetism on the mechanical properties of NiFeCoCrMn alloys [19]. These interesting results notwithstanding, the fact that supercell and CPA calculations produce such divergent magnetic structures calls into question the validity of the results using the conventional CPA approach.

Here we employed a two-Mn model using CPA that distinguishes two types of Mn species—with opposite spin orientations but equal concentration. A similar approach has been applied to NiMn alloys by Akai *et al.* [30]. We showed that this approach successfully recovers both antiparallel spin alignments and large Mn moments found in supercell calculations [20]. Furthermore, it is found that the two-Mn model is energetically favorable to the conventional one-Mn model [20]. Given that CPA methodology is specifically designed to describe the configurational averaged physical observable in the thermodynamic limit, it is desirable to justify the two-Mn model obtained from CPA by comparing the electronic structure and magnetism with supercell calculations. In addition, using a suitable model Hamiltonian to study the spin thermodynamics based on the ground-state two-Mn model, we can further elucidate magnetic properties at finite temperature and pressure, and assess the effect of magnetism on electronic transport properties.

The paper is organized as follows: computational details are described in Sec. II. Then, the electronic structure calculations for the ground magnetic state are presented in Sec. III A. Spin spiral calculations are performed in Sec. III C to sample the spin noncollinear configurations and to verify the validity of mapping magnetic interactions onto a Heisenberg Hamiltonian. The isotropic exchange parameters within the Heisenberg model are calculated in Sec. III B, based on which thermodynamic simulations are performed in Sec. III D. The finite-temperature transport properties are explored with the temperature-dependent spin disorder, and temperature-dependent atomic displacement is considered in Sec III E. In Sec. III F, the magnetism and residual resistivity are calculated as a function of hydrostatic pressures.

II. METHODOLOGY

A. Computational details

Two different methods have been used to perform first-principles calculations for alloys: the supercell method and the Korringa-Kohn-Rostoker Green's function method [31,32] combined with CPA [27] (hereafter called KKR-CPA).

The supercell calculations were carried out using the projector augmented wave method (PAW) [33] as implemented in the Vienna Ab Initio Simulation Package (VASP) [34,35]. To mimic the disordered local environment, we constructed several conventional cubic special quasirandom structures (SQSs) [26] with 108 atoms included. We used a kinetic energy cutoff of 400 eV for the plane-wave expansion and a Γ-centered Monkhorst-Pack grid [36] for the Brillouin zone (BZ) integration. The ionic coordinates were relaxed while keeping the cubic cell shape and volume fixed at the experimental value for NiCoMn alloys, with lattice parameter $a = 3.60$ Å [9]. To give an accurate prediction of atomic displacements, the generalized gradient approximation (GGA) parametrized by Perdew, Burke, and Ernzerhof (PBE) [37] was used for the exchange and correlation. Employing the optimized structure, the electronic structure and magnetic properties were further calculated using the local density approximation (LDA). Methfessel-Paxton smearing of 0.1 eV and a Γ-centered 3×3×3 (4×4×4) k-point mesh were used for ionic relaxation [density of states (DOS) calculations] within the 108-atom SQS cell. A spin collinear configuration was assumed.

The KKR-CPA method as implemented in the Munich SPR-KKR package [38] was used to calculate the effect of disorder on the electronic structure and resistivity. Consistent with the supercell electronic structure calculations, the LDA has been employed for the exchange and correlation, and the experimental lattice parameter was adopted. The potential is described within the atomic sphere approximation (ASA). The angular momentum expansion of the Green's function employed a cutoff of $l_{\max} = 4$.

Employing the self-consistent Green's function, the conductivity tensor is calculated by using the linear-response Kubo-Greenwood formula [39,40] with the configurational averaged state described within the CPA [41]:

$$\sigma_{\mu\nu} = \frac{\hbar}{\pi N \Omega} \mathrm{Tr}\left\langle j_\alpha^\mu \mathrm{Im}G^+(E_F) j_\beta^\nu \mathrm{Im}G^+(E_F)\right\rangle, \qquad (1)$$

where j_α^μ denotes the μ-component of the current density operator j for species α with concentration c_α, and $G^+(E_F)$ is the retarded Green's function at the Fermi energy. To study the effect of displacement scattering and spin disorder on ρ_0, we used the so-called alloy analogy model (AAM) to calculate the configurational average over a discrete set of species-resolved atomic displacements and local moment orientations [42]. Two types of atomic displacements are distinguished: static atomic displacements (denoted as u_0), arising from the local atomic relaxation, and thermal atomic displacements [denoted as $u(T)$], arising from the thermally induced lattice vibrations. The former were calculated from the structurally optimized supercell, while the latter were estimated from the temperature-dependent root-mean-square displacements

calculated using the Debye model (see Ref. [42] for details). The u_0 and $u(T)$ are assumed to be additive.

B. Magnetism

To evaluate the equilibrium spin configuration in the NiCoMn alloy, the classical Heisenberg model is used, with the following form of the Hamiltonian:

$$\hat{H} = -\sum_{i,j}^{\mu,\nu} c_\mu c_\nu J_{i,j}^{\mu,\nu} \mathbf{e}_i^\mu \cdot \mathbf{e}_j^\nu. \tag{2}$$

Here the vectors $\mathbf{e}_i^\mu$ represent the normalized spin moments (or reduced moments) on site i occupied by species μ, c_μ is the concentration of species μ, and $J_{i,j}^{\mu,\nu}$ are the exchange parameters between site i (occupied by species μ) and site j (occupied by species ν). The parameters $J_{i,j}^{\mu,\nu}$ are calculated using the so-called Lichtenstein formula [43] as implemented in SPR-KKR. The summation over atomic species (μ, ν), randomly distributed over lattice sites, is weighted with their respective concentrations (c_μ, c_ν). As defined here, positive (negative) exchange parameters favor ferromagnetic (antiferromagnetic) spin alignments. We note that in Eq. (2), the exchange parameters account for the interatomic exchange interactions scaled with the size of the magnetic moments of the interacting atoms.

C. Thermodynamics

The finite-temperature magnetic properties are investigated using classical mean-field theory, the classical pair cluster approximation, and classical Monte Carlo simulations. The mean-field approximation is expected to be reasonable due to the large coordination number for the nearest spin interactions—12 within the first fcc coordination shell. Moreover, Monte Carlo simulation is also employed to estimate the correlation effect. A rigid spin approximation was used to treat magnetic moments of $3d$ transition-metal ions, which are considered as classical vectors.

The magnetization at finite temperature can be described within classical mean-field theory by the solution of the matrix equation:

$$\langle \hat{e}_z \rangle = L(\beta \hat{h}_{\text{eff}}), \tag{3}$$

$\hat{e}_z$ is the matrix for reduced moments (projected to the quantization axis z), which is a column vector whose components are the z component of the reduced moment on each species μ, $\mathbf{e}_z^\mu$. $\langle \cdots \rangle$ represents the thermodynamics average over the spin orientations at all sites. $L(x)$ is the Langevin function, whose argument $x = \beta h_{\text{eff}}$ is the distribution function for the spin orientation at a certain temperature T. β is $\frac{1}{k_B T}$, where k_B is the Boltzmann constant, and $\hat{h}_{\text{eff}}$ is the effective Weiss field matrix with argument h_{eff}^μ for species μ. Specifically, $h_{\text{eff}}^\mu = \sum_\nu c_\nu \sum_j J_{i,j}^{\mu,\nu} \langle (\mathbf{e}_j^\nu)_z \rangle$. The critical temperature corresponds to the vanishing of $\langle \mathbf{e}_z^\mu \rangle$ for all species μ.

In addition, two techniques that allow us to incorporate spin correlations beyond the single-site approximation—the cluster variation method (CVM) [44,45] and Monte Carlo simulation—have been employed. The CVM was used to calculate the thermodynamic quantities in alloys. The traditional approach—the mean-field approximation (MFA)—usually overestimates the critical temperature and fails to predict stability of the correct phase. This failure is caused by the presence of strong nearest-neighbor interactions and, as a result, strong interatomic correlations that are neglected in MFA. To incorporate the correlation effect, cluster techniques are used. In these techniques, the interactions within the maximal size cluster and its subclusters are incorporated exactly, while the interactions of the cluster with the rest of the system are described through the effective field. The two mostly popular cluster methods are the cluster variation and cluster field methods (CVM [44,45] and CFM [46], respectively). Both methods are equivalent to each other in the case of the pair cluster approximation. Our calculation of the critical temperature of the Heisenberg model was executed using pair clusters CFM [47].

Parallel tempering Monte Carlo simulations [48,49] are also employed to obtain the finite-temperature magnetic state. The Heisenberg Hamiltonian $\hat{H} = -\sum_{i,j}^{\mu,\nu} J_{i,j}^{\mu,\nu} \mathbf{e}_i^\mu \cdot \mathbf{e}_j^\nu$ is employed for a finite-size cell, with the spins randomly distributed according to the concentration. A swap trial is performed with a METROPOLIS-like probability that satisfies the detailed balance condition. The transition probability from a configuration X_m simulated at temperature T_m to a configuration X_n simulated at temperature T_n is

$$W(X_m, T_m | X_n, T_n) = \min[1, \exp(-\triangle)], \tag{4}$$

$$\triangle = (1/k_B T_n - 1/k_B T_m)(\hat{H}_m - \hat{H}_n). \tag{5}$$

To take into account the effect of the critical slowing down near the phase transition, we also apply the Wolff cluster update algorithm [50]. Given a randomly chosen direction $\hat{n}$, spins are iteratively added to the flipping cluster with probability

$$p = 1 - \exp\left\{\min\left[0, \frac{2J_{ij}}{k_B T}(\hat{n} \cdot \mathbf{e}_i)(\hat{n} \cdot \mathbf{e}_j)\right]\right\}, \tag{6}$$

and then the cluster of spins is flipped with respect to the hyperplane orthogonal to $\hat{n}$. Therefore, a typical Monte Carlo step consists of a single spin flip trial for every spin, a cluster update for the whole system, and a replica swapping trial between neighboring temperatures.

III. RESULTS AND DISCUSSIONS

A. Electronic structure

A previous CPA study [20] found multiple magnetic states of NiCoMn that are close in total energy. Different magnetic states are distinguished depending on the spin orientation of the Mn local moment. Specifically, a state with all Mn spins parallel (antiparallel) with the Co spins was found, and is denoted as the FM (AFM) state, with only one type of Mn spin in either case. Alternatively, it has been demonstrated that the magnetic ground state corresponds to a state that distinguishes two types of Mn moments ($\text{Mn}^\uparrow$ and $\text{Mn}^\downarrow$) with roughly equal populations but opposite spin orientations [20]. This is analogous to the so-called disordered local moment (DLM) state [51], with the local moment disorder only applied to Mn. For brevity, this ground state is denoted as the DLM-Mn state.

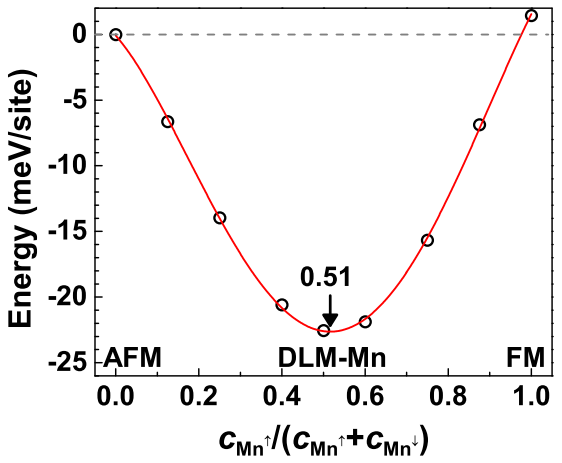

FIG. 1. Total energy (meV/site) as a function of $c_{Mn^\uparrow}/(c_{Mn^\uparrow}+c_{Mn^\downarrow})$. The zero energy corresponds to the energy of the AFM state. The black arrow labels the energy minimum at $c_{Mn^\uparrow}/(c_{Mn^\uparrow}+c_{Mn^\downarrow})=0.51$.

Using the binary pseudoalloy approximation with uncompensated collinear "up" and "down" Mn moments [30], i.e., uncompensated DLM, Fig. 1 illustrates the total energy change as a function of the relative ratio of $Mn^\uparrow$ to the total Mn, defined as $c_{Mn^\uparrow}/(c_{Mn^\uparrow}+c_{Mn^\downarrow})$, where $c_{Mn^\uparrow}$ and $c_{Mn^\downarrow}$ are the concentrations of $Mn^\uparrow$ and $Mn^\downarrow$, respectively. $c_{Mn^\uparrow}/(c_{Mn^\uparrow}+c_{Mn^\downarrow})=0, 0.5, 1$ correspond to the AFM, the DLM-Mn, and the FM states, respectively. As seen from Fig. 1, the energy minimum of NiCoMn at $c_{Mn^\uparrow}/(c_{Mn^\uparrow}+c_{Mn^\downarrow})=0.51$ occurs around the DLM-Mn state, thus we simply regard the DLM-Mn state as the ground state. Since both the AFM and the FM states have higher energies than the DLM-Mn ground state and the AFM state is slightly more energetically favorable than the FM state, we restrict ourselves to the comparison of the AFM state and the DLM-Mn state.

Besides the different spin orientations, different magnetic states obtained from KKR-CPA also possess distinct magnitudes of the local moments, particularly for Mn. For instance, a Mn moment as large as $2.20\mu_B$ is found in the DLM-Mn state while the local moment on Mn in the AFM state is only $0.75\mu_B$. To verify the magnetic features (orientation and magnitude of the local moments) obtained from CPA, supercell spin collinear calculations were performed as a benchmark. Similar to the DLM-Mn state, the supercell calculation distinguishes two types of Mn local moments, with large local moment magnitude but opposite spin orientations: ~50% $Mn^\uparrow$ and ~50% $Mn^\downarrow$. This feature is insensitive to the choice of exchange-correlation functional (LDA or GGA).

We further compare the electronic structure from the supercell method and the CPA to validate the KKR-CPA ground state. Figure 2 illustrates the total density of state (DOS) and species-resolved partial DOS (pDOS) using both the supercell (black lines) and CPA methods. Two CPA solutions—DLM-Mn state (blue lines) and AFM state (green lines)—are considered here. Figure 2(a) compares the total DOS. Notably, because the CPA directly provides the configurational averaged DOS, the fine structure of DOS as in the supercell calculations is washed out. In addition, the total DOS of the DLM-Mn state

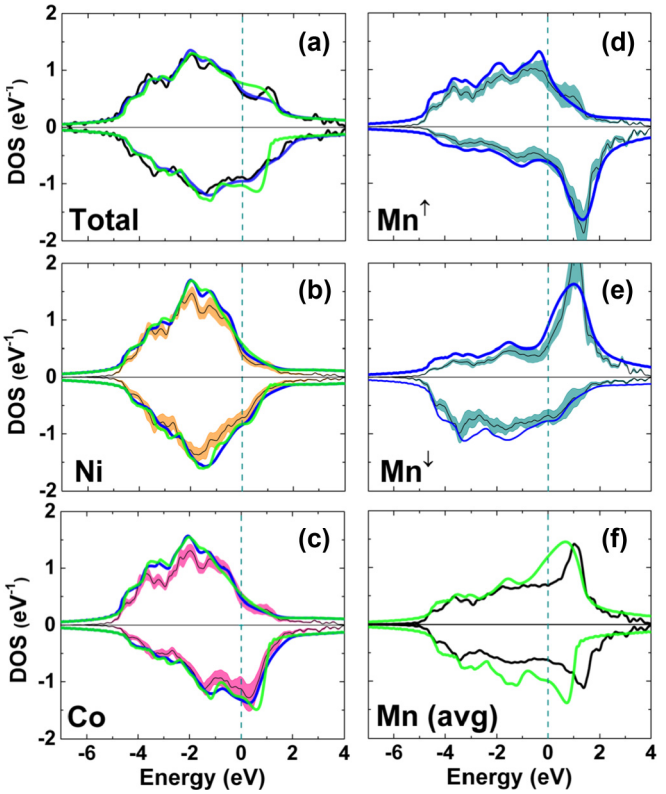

FIG. 2. (a) Total DOS (states/eV/site) and (b)–(f) species-resolved partial DOS (states/eV/site) of NiCoMn random alloy using the supercell method (black lines) and the CPA method that produces two states: the DLM-Mn state (blue lines) and the AFM state (green lines). In the supercell method, the black lines correspond to the averaged DOS in each case while their colored smearing of the partial DOS gives the standard deviation of the partial DOS at each energy point. This is obtained from sampling the partial DOS of all atoms with the same species in the supercell. (d), (e) $Mn^\uparrow$ and $Mn^\downarrow$ distinguish Mn with up spins and down spins, respectively. (f) Averaged Mn partial DOS from supercell method (black lines) and from the AFM state in CPA (green lines). All DOS plots are rescaled per atom, and the Fermi level (dashed green line) is shifted to zero energy.

is consistent with the corresponding density of state obtained from the supercell calculation, while the AFM state displays enhanced DOS around the Fermi energy, and in particular, a shallow peak in the minority-spin channel shows up just above the Fermi energy.

As for the species-resolved pDOS, Figs. 2(b) and 2(c) shows pDOS of 3*d* states for Ni and Co species. The black line indicates the averaged DOS obtained from the supercell calculation, and the colored smearing—quantified by the standard deviation of the DOS at each energy point—encapsulates the fluctuations of the density of states at different Ni (Co) sites due to the different chemical environment of each site and local atomic relaxations that result from it. Both CPA solutions show pDOS of Ni and Co consistent with the supercell method. The on-site exchange splitting on Ni—with nearly filled 3*d* bands—is small as is the Ni moment. On the contrary, having one less valence electron, the on-site Hund's

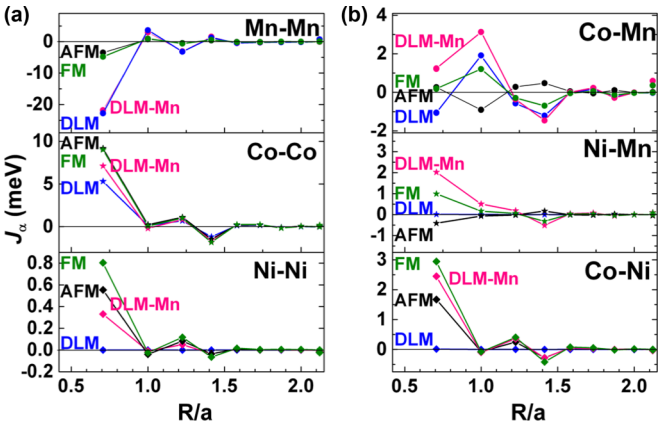

FIG. 3. The intraspecies (a) and interspecies (b) exchange parameters (J_α) as a function of bond length (for a certain αth nearest-neighboring shell) in random alloy NiCoMn in the following multiple states: FM state, AFM state, DLM state, and DLM-Mn state. In the DLM-Mn state and DLM state, only the interactions centered around a spin-up Mn atom are shown.

exchange is stronger in Co, therefore producing a more sizable Co moment ($\sim 1\mu_B$).

As was shown in a previous study [20], the Mn moments fall into two categories: large positive ($Mn^{\uparrow}$) and large negative ($Mn^{\downarrow}$). In addition, the local moment distributions of each species in the NiCoMn supercell have only modest fluctuations: the half-width at half-maximum (HWHM) of the species-resolved moment distributions are $\sim 0.3\mu_B$ for Ni, $\sim 0.4\mu_B$ for Co, $\sim 0.5\mu_B$ for $Mn^{\downarrow}$, $\sim 0.6\mu_B$ for $Mn^{\uparrow}$. In Figs. 2(d) and 2(e), both averaged pDOS of $Mn^{\uparrow}$ and $Mn^{\downarrow}$ from the supercell method are compared with that in the DLM-Mn state. Again, the DLM-Mn state agrees with the supercell calculation and captures the important magnetic signature: large Mn local moments but opposite Mn spin orientations. Unlike the single-site CPA, the supercell calculation includes the effect of the local atomic displacements. The agreement of the DOS between the supercell and CPA methods suggests that the local atomic displacements in the NiCoMn alloy have a very minor effect on the averaged DOS.

In contrast, Fig. 2(f) shows that the averaged Mn pDOS of the AFM state is not consistent with the supercell method, particularly the DOS at the Fermi energy. A large Mn pDOS at the Fermi energy in the AFM state is observed, suggesting a Stoner's instability toward the formation of a larger Mn moment rather than the $0.8\mu_B$ that actually is found in the AFM state.

In summary, the single-site CPA approach, which assumes only one type of Mn atoms, gives an inconsistent prediction of the local moments and electronic structure, as compared with the supercell calculation. In addition, it may also suffer from magnetic instability due to interatomic exchange interactions. This issue is discussed in the following two subsections.

B. Heisenberg exchange interactions

The isotropic exchange parameters are calculated for different magnetic states: FM, AFM, DLM, DLM-Mn, as defined previously. Figures 3(a) and 3(b) illustrate the calculated intraspecies (between the same species type) and interspecies (between different species types) exchange interactions as a function of interatomic distance (scaled by the lattice parameter). Here we use J_α to denote the exchange parameters characterizing interactions within the αth nearest atomic shell. As expected, J_α display long-range RKKY-like oscillations—between positive (ferromagnetic coupling) or negative (antiferromagnetic coupling) values—and decrease with increasing distance. The J_α become negligibly small beyond the seventh-nearest-neighbor shell. We note that since the Ni moment collapses in the DLM state, the corresponding inter- and/or intraspecies exchange couplings vanish accordingly.

It is found that the intraspecies exchange interactions are predominately determined by the first-nearest-neighbor exchange interactions: Co-Co and Ni-Ni exchange interactions are ferromagnetic, whereas the Mn-Mn interactions are antiferromagnetic regardless of different magnetic states. While the $J_1^{\text{Co-Co}}$, $J_1^{\text{Ni-Ni}}$ are only modestly modified by different magnetic states, the $J_1^{\text{Mn-Mn}}$ is found to be sensitive to the specific magnetic states. In particular, while $J_1^{\text{Mn-Mn}}(\text{AFM}) \sim J_1^{\text{Mn-Mn}}(\text{FM})$ and $J_1^{\text{Mn-Mn}}(\text{DLM}) \sim J_1^{\text{Mn-Mn}}(\text{DLM-Mn})$, $J_1^{\text{Mn-Mn}}$ (DLM-Mn) is one order of magnitude greater than $J_1^{\text{Mn-Mn}}$ (AFM).

As for the interspecies exchange coupling, the Ni-Co interactions are dominated by the nearest-neighbor interaction (J_1) that favors ferromagnetic coupling. This is also true for Ni-Mn interactions. As for Co-Mn interactions, J_2 becomes dominant and the sign of J_α become more sensitive to the specific magnetic states.

It is worth noting that the exchange parameters between different species at different sites can fluctuate due to different disordered local environments, variation of the bond length due to the local relaxation, and the fluctuation of the size of the moments for each species [52]. Even though the moment size fluctuations turn out to be mild for each species, which may suggest relatively small variation of the exchange parameters, their actual fluctuations are worth a more detailed investigation. However, this is beyond the scope of this work. Here we employ the (configurationally averaged) exchange parameters to explore the thermodynamic properties.

C. Spin spiral calculation

To investigate the stability of the collinear magnetic state with respect to the formation of a noncollinear magnetic structure, and the applicability of the Heisenberg model, we carried out spin spiral calculations using the CPA method. The single-site treatment of the spin spiral state in a disordered alloy, based on the generalized Bloch theorem [53,54], was implemented in SPR-KKR by Mankovsky *et al.* [55]. The self-consistent spin spiral calculation shows the relative energy scale of the collective excitation—spin wave—and the single-particle excitation—Stoner excitation. We constrained the spin spiral vector, denoted as $\mathbf{q}$, along $[\zeta, 0, 0]$, $[\zeta, \zeta, 0]$, and $[\zeta, \zeta, \zeta]$ directions in reciprocal-lattice units (r.l.u.) to sample the Γ to X, X to Γ, and Γ to L branches of the fcc BZ. The orientation of the averaged local moment of a disordered magnetic alloy can be written as $(\sin\Omega\cos\Phi, \sin\Omega\sin\Phi, \cos\Omega)$ in the general spherical coordination, where Ω and Φ are the polar angle and the azimuthal angle, respectively. We

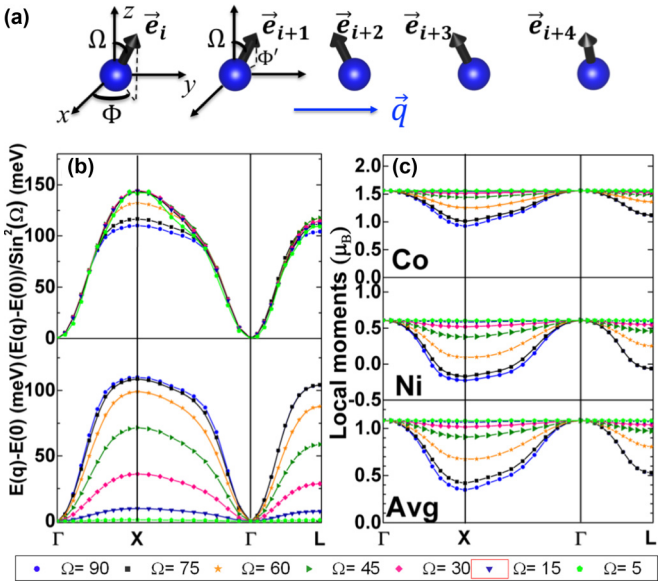

FIG. 4. (a) Sketch of the spin spiral state, propagating along the y direction for an artificial one-dimensional atomic chain (blue spheres). (b) Adiabatic magnon energy (upper panel), defined as $\frac{E(\mathbf{q})-E(0)}{\sin^2(\Omega)}$, given in meV/site, and spin spiral energy (lower panel), defined as $E(\mathbf{q}) - E(0)$, given in meV/site, in NiCo solid solution alloy for different cone angles Ω (given in degrees). The spin spiral vector $\mathbf{q}$ is along Γ-X $[\zeta, 0, 0]$, X-Γ $[\zeta, \zeta, 0]$, and Γ-L $[\zeta, \zeta, \zeta]$ direction. (c) Species-dependent local moments (μ_B) and averaged net moment (μ_B) for different spin spiral vectors.

studied a cone type of spin spiral state that propagates along the $\mathbf{q}$ direction with a fixed spin cone angle Ω but a modulated azimuthal angle Φ along the $\mathbf{q}$ direction: Φ increases by $\mathbf{q} \cdot (\mathbf{r}_i - \mathbf{r}_{i+1})$ between site i (at $\mathbf{r}_i$) and site $i + 1$(at $\mathbf{r}_{i+1}$) [see Fig. 4(a) for a sketch]. Note that in CPA, it is the *average moment* that propagates along $\mathbf{q}$. For multicomponent alloys, the spin collinearity between different species on one site is enforced, while the spin noncollinearity between averaged moments on different sites is allowed and can be represented by the spin spiral state.

Two different definitions of the low-energy excitation and the local moments are studied in order to explore the energetic and magnetic properties in the spin spiral state. First, $E(\mathbf{q}) - E(0)$ is calculated as the spin spiral energy. An additional normalized spin spiral energy, $[E(\mathbf{q}) - E(0)]/\sin^2(\Omega)$, is also investigated at different Ω and can be interpreted as the adiabatic magnon energy or frozen magnon energy [56]. If the magnetic interactions of the alloy are well described by the Heisenberg model, then $[E(\mathbf{q}) - E(0)]/\sin^2(\Omega)$ is independent of the polar angle Ω [56,57]. Using the NiCo alloy as an example, Figs. 4(b) and 4(c) illustrate the self-consistent spin spiral energy and the corresponding moment evolution for a set of cone angles Ω. Concentrating on the moment evolution at different spin spiral vectors, we note two important features. On the one hand, in the long-wavelength limit ($\mathbf{q} \to \mathbf{0}$), the Ni and Co local moments are stable against the spin noncollinearity, as the spin wave excitation energy is well below the energy scale of Stoner excitations. On the other hand, for large $\mathbf{q}$, approaching the short-wavelength limit, the magnitude of the local moments on both Ni and Co atoms

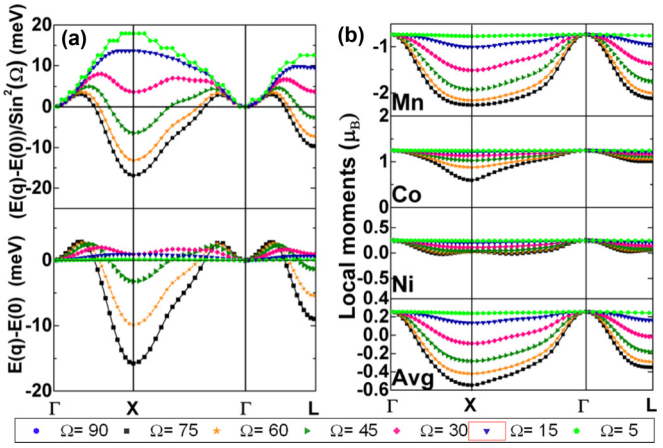

FIG. 5. (a) Adiabatic magnon energy (upper panel) and spin spiral energy (lower panel) in NiCoMn (AFM state) for different cone angle Ω (given in degrees). The spin spiral vector $\mathbf{q}$ is along the Γ-X $[\zeta, 0, 0]$, X-Γ $[\zeta, \zeta, 0]$, and Γ-L $[\zeta, \zeta, \zeta]$ directions. (b) Species-dependent local moments and averaged net moment for different spin spiral vectors.

starts to reduce, since the increased spin-wave excitation energy approaches the spin-flipping Stoner excitation region. We note that this moment reduction is more pronounced for larger Ω since the angle between successive spins is larger. In particular, $\Omega = 90^\circ$, corresponding to an antiferromagnetic helix state, gives rise to the largest moment change. A similar analysis can be performed for NiCoMn alloys.

In Figs. 5 and 6, we compare the spin spiral energy and local moment pattern of the NiCoMn alloy in both AFM and DLM-Mn states. In the AFM state, the magnitude of the Mn local moment increases by a factor of 3 from the Γ-point toward the BZ boundary (X point), exhibiting a striking longitudinal spin fluctuation that is also predicted by Niu *et al.* [19]. The moment size fluctuation is associated with a modest

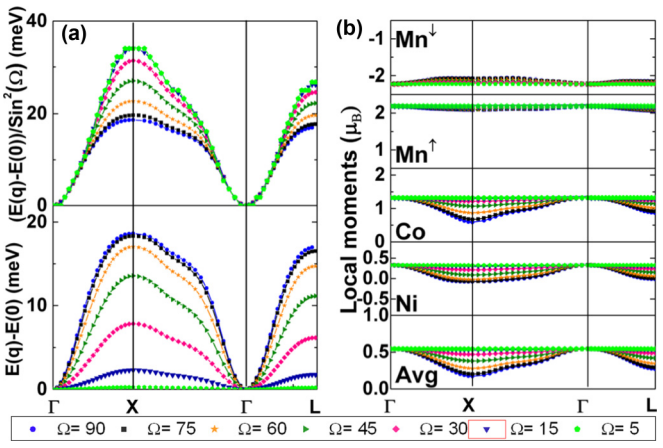

FIG. 6. (a) Adiabatic magnon energy (upper panel) and spin spiral energy (lower panel) in NiCoMn (DLM-Mn state) for different cone angle Ω (given in degrees). The spin spiral vector $\mathbf{q}$ is along Γ-X $[\zeta, 0, 0]$, X-Γ $[\zeta, \zeta, 0]$, and Γ-L $[\zeta, \zeta, \zeta]$ direction. (b) Species-dependent local moments and averaged net moment for different spin spiral vectors. Two types of Mn species are distinguished using Mn$^\sigma$, where $\sigma = \uparrow$ or $\downarrow$ denote the spin orientation.

energy reduction, ∼15 meV/site at $\Omega = 75°$. Note that the spin spiral energy of the AFM state is not continuous and is not well defined at $\Omega = 90°$ due to a low-spin to high-spin transition, and is not shown here. The negative spin spiral energy at finite q indicates that the collinear AFM state is not energetically stable, compared with the spin noncollinear state with a spin spiral vector $\mathbf{q} = [\zeta, 0, 0]$ r.l.u. The typical Stoner excitation reduces the size of the local moment in the presence of spin noncollinearity. However, here the local Mn moments in the AFM state behave oppositely—increasing the local moments with spin noncollinearity. This is because the collinear AFM state is highly frustrated due to the fact that the Mn local moments between different sites are constrained to be parallel.

As opposed to the AFM state, the spin spiral of the DLM-Mn state at the Γ point is the most energetically favorable (see Fig. 6). Moreover, in the long-wavelength limit, $\zeta \leqslant 0.4$ along the $[\zeta, 0, 0]$ direction, $[E(q) - E(0)]/\sin^2(\Omega)$ is independent of Ω, evidently supporting the applicability of the Heisenberg model in the vicinity of the DLM-Mn state. As for the local moments, the size of the local moments on Mn in this spin spiral state is relatively insensitive to the spin spiral vector and different cone angles: Mn spins are only reduced by 5% at the zone boundary (see Fig. 6). Here, in the DLM-Mn state, the strongest moment reduction comes from Co moments, whose spins decrease by 50% at the zone boundary. The relative insensitivity of the spin sizes to the spin noncollinearity validates the usage of the Heisenberg model. Therefore, the thermodynamic simulation based on the Heisenberg model is only applicable for the DLM-Mn state. In the succeeding section, we explored the thermodynamics of NiCoMn using the exchange parameters (J_{ij}) from the DLM-Mn state.

D. Thermodynamics

We employ the Heisenberg model to describe the magnetic interactions, based on the J_{ij} from the DLM-Mn state. In the DLM-Mn state, all the local moments, particularly Mn moments, do not exhibit strong size fluctuations, justifying the applicability of Heisenberg interactions in the assumption of rigid classical spins. We use the classical Monte Carlo simulations to calculate the critical temperature (T_c), and we compare the T_c predictions with other approximations, such as the classical pair cluster approximation and the classical mean-field approximation. Progressing from MF to PC, and further to MC, the spin correlations are gradually taken into account—MF has no spin correlation effect, PC only includes the pairwise correlations, and MC takes all correlations into consideration. The critical temperatures are $T_c^{\mathrm{MF}} = 343$ K, $T_c^{\mathrm{PC}} = 320$ K, and $T_c^{\mathrm{MC}} = 219$ K, respectively. Figure 7(d) also illustrates the finite-size effect in classical MC using an 8×8×8, 12×12×12, and 16×16×16 cubic cell, and evidently good convergence of T_c^{MC} has been reached. The reduction of T_c from MF to PC is only 23 K. Since PC only includes the pairwise correlations compared with the MF, the small reduction of T_c indicates that the correlation effect within the pair cluster is not significant. On the other hand, T_c^{MC} is reduced by (appreciably) 31% compared with T_c^{PC}, suggesting an important correlation effect within the high-order clusters.

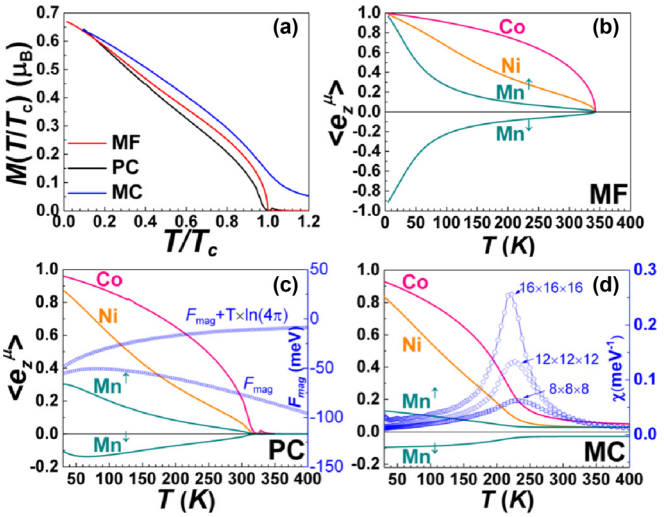

FIG. 7. (a) Simulated net magnetization $M(T)$ (μ_B/site) as a function of reduced temperature (T/T_c) using three different statistical approximations: classical mean-field approximation (MF), classical pair cluster approximation (PC), and classical Monte Carlo (MC). The temperature-dependent reduced species-resolved magnetization ($\langle e_z^{\mu} \rangle$) in (b) classical mean-field approximation, (c) classical pair cluster approximation, and (d) classical Monte Carlo approximation. Magnetic free energy (F_{mag}, meV/site) and the magnetic interaction energy ($F_{\mathrm{mag}} + T \times \ln 4\pi$, meV/site) of NiCoMn in DLM-Mn state are plotted in (c) using PC. The temperature-dependent magnetic susceptibility using 8×8×8, 12×12×12, and 16×16×16 cubic cells are displayed in (d) using MC.

Unfortunately, there is no experimental value available for T_c in the NiCoMn alloy.

The temperature dependence of the total magnetization [$M(T)$, μ_B/site] obtained using the three different statistical approximations is shown in Fig. 7(a). The variations in the shapes of the magnetization curves are similar in all three approaches. Figures 7(b)–7(d) illustrate the reduced species-resolved magnetization ($\langle e_z^{\mu} \rangle$) in different statistical approximations. We find that the $\langle e_z^{\mathrm{Co}} \rangle$ is relatively stable while the $\langle e_z^{\mathrm{Mn}} \rangle$ drops quickly with temperature due to disordered Mn moments even at low temperature. In addition, Fig. 8 shows a zoom-in of a representative spin configuration for a 12×12×12 cubic cell, simulated by classical MC at 20 K. First, the Mn moments (blue and light blue arrows) are disordered with random angular distribution. As opposed to Mn moments, the Ni moments (silver arrows) and Co moments (red arrows) are (approximately) collinearly aligned. The reason for the observed disordered Mn moments is that the effective exchange field on Mn is small. This is because the Weiss fields from the neighboring $\mathrm{Mn}^{\uparrow}$ and $\mathrm{Mn}^{\downarrow}$ have opposite signs, compensating for each other (see Table I). As opposed to the small effective exchange field on Mn, those on Ni and Co are much stronger. The effective exchange fields on each species ($J_0^{\mu} = \sum_{\nu} c^{\nu} J_0^{\mu,\nu}$) and the effective exchange field between species pairs ($J_0^{\mu,\nu} = \sum_j J_{ij}^{\mu,\nu}$) are listed in Table I. From this discussion, it is clear that the magnetic critical temperature is mainly determined by the effective exchange field on the Ni and Co species.

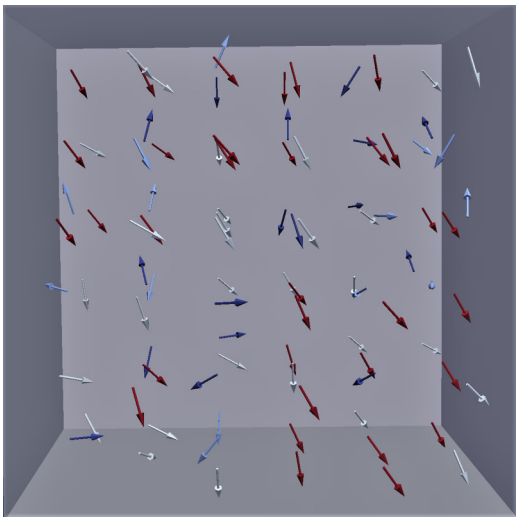

FIG. 8. A zoom-in of a representative spin configuration at 20 K for the DLM-Mn state, taken from a large $12\times12\times12$ unit cell. Red arrows indicate Co spins, sliver arrows denote Ni spins, and blue and light blue arrows are local moments on $Mn^{\uparrow}$ and $Mn^{\downarrow}$.

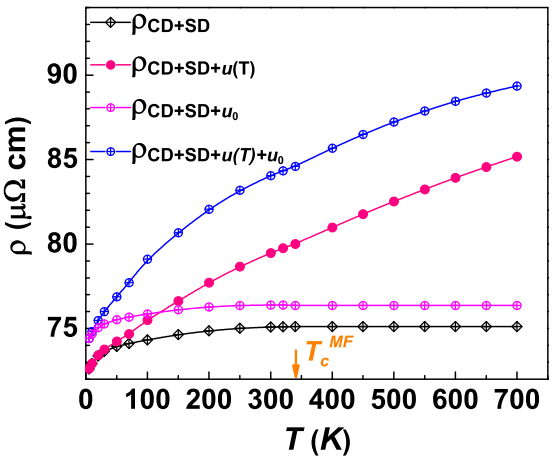

FIG. 9. Resistivity of NiCoMn alloy at finite temperatures, $\rho(T)$, given in units of $\mu\Omega$ cm. Electron scattering due to the static displacements (u_0), thermal displacements [$u(T)$], and spin disorder (SD) are considered either separately or with different combinations (see the main text for details). The chemical disorder (CD) is always included. The mean-field transition temperature (T_c) is also labeled.

In contrast, the exchange interactions of the AFM state yield a much smaller magnetic critical temperature ($T_c^{\mathrm{MF}} = 243$ K), as compared with that based on the DLM-Mn state: $T_c^{\mathrm{MF}} = 343$ K. This difference mainly comes from the negative and unstable $J_0^{\mathrm{Co,Mn}}$ contribution to the net effective exchange field in the AFM state. It is therefore anticipated that the AFM state adversely affects the Gibbs free energy through the erroneous magnetic contributions.

E. Resistivity at finite temperature

The electronic structure of the multiple metastable states of NiCoMn has a striking effect on the residual resistivity (ρ_0): ρ_0 in the DLM-Mn state is 40% greater than that in the one-Mn state in KKR-CPA [20]. Here we start from the residual resistivity and explore the transport properties at finite temperatures by including the atomic displacements and the transverse spin fluctuations. First, as previously introduced in Sec. II, we consider two types of atomic displacements—static displacements (u_0) and thermal displacements [$u(T)$]. The averaged magnitudes of static displacements for each species were calculated from the supercell calculations. Thermal displacements, i.e., the mean-square root displacements, are calculated using the Debye model (see Ref. [42]). At finite temperature, the thermal displacements are added to the static displacements at finite temperatures [i.e., $u_{\mathrm{tot}} = u_0 + u(T)$]. In addition, the transverse spin fluctuations at a given temperature are simulated by using type-dependent $\langle \mathbf{e}_z^{\mu} \rangle$ within the classical mean-field simulations [Fig. 7(b)]. The resistivity due to these different scattering mechanisms is then calculated based on the above approximation.

TABLE I. The effective exchange interactions between species-pairs (μ, ν) $J_0^{\mu,\nu}$ (meV) and the effective exchange field on species (μ) J_0^{μ} (meV) are given. See the main text for definitions and details.

	Ni	Co	$Mn^{\uparrow}$	$Mn^{\downarrow}$
Ni	8.28	34.9	24.9	−20.5
Co	34.9	122.4	0.32	16.9
$Mn^{\uparrow}$	24.9	0.32	−327.4	332.6
$Mn^{\downarrow}$	−20.5	16.9	332.6	−328.3
J_0^{μ}	15.1	55.3	9.3	−0.5

Figure 9 illustrates $\rho(T)$ in four different cases with different electron scattering mechanisms included: (i) temperature-dependent spin disorder; (ii) temperature-dependent spin disorder and thermal displacements; (iii) static displacements and temperature-dependent spin disorder; (iv) in the presence of the static displacements, thermal displacements, and temperature-dependent spin disorder. We note that the electron scattering due to the intrinsic chemical disorder (CD) is always included. Assuming that Matthiessen's rule (MR) is valid, the scattering due to each individual scattering mechanism can be separated out. We first emphasize that no matter whether the static displacements are included or not, the additional electron scattering due to transverse spin fluctuation is weak. Here we define the spin disorder resistivity (ρ^{SDR}) as the resistivity enhancement when all spins are fully disordered ($T > T_c$). We found small values for $\rho^{\mathrm{SDR}} - \rho^{\mathrm{SDR}}(u_0 = 0) = 2.5\ \mu\Omega$ cm and $\rho^{\mathrm{SDR}}(u_0) = 2.0\ \mu\Omega$ cm, as seen in Fig. 9. The underlying reason for the smallness of forgoing quantities is that, even at $T = 0$ K, the "local moment" scattering attendant to two antiparallel Mn spin models, over and above the large chemical disorder scattering, results in a Fermi surface that is already so washed-out (smeared out in **k**-space) that introducing additional spin disorder scattering has a negligible effect. Due to the weak magnetic scattering in NiCoMn, $\rho(T)$ does not display a distinct kink at T_c, as in ferromagnetic Ni, Fe, NiFe, NiCo, and NiFeCo [21,42,58]. Furthermore, the static displacements raise the residual resistivity by 1.8 $\mu\Omega$ cm, which is comparable to ρ^{SDR}.

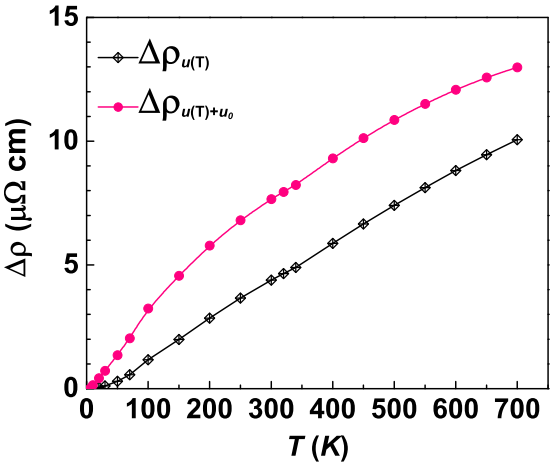

FIG. 10. The resistivity enhancement [$\Delta\rho(T)$, $\mu\Omega$ cm] due to the effect of thermal displacements [$u(T)$], with (red dots) and without (black diamonds) taking into account the static displacements (u_0).

The thermal displacements have a notable effect on the resistivity enhancement. Figure 10 illustrates the thermal-displacement-induced resistivity enhancements ($\Delta\rho$) as a function of temperature when static displacement is included (red dots) or not (black diamonds). In the absence of the static displacements, the thermal-displacement-induced resistivity enhancement $\Delta\rho_{u(T)}$ increases slowly in the low-temperature region ($T < 50$ K), but increases linearly in the high-temperature region—beyond the Debye temperature (T_D). This temperature dependence is normally expected in nonmagnetic metals. However, despite the fact that static displacements have a small effect on raising ρ_0, they affect the temperature-dependent resistivity remarkably when combined with the thermal displacements. At low temperatures, $\Delta\rho_{u(T)+u_0}$ increases more rapidly with temperature than $\Delta\rho_{u(T)}$. This is due to the fact that the coupling between the u_0 and $u(T)$ contributes a $u_0 \times u(T)$ term in the expansion of u^2_{tot}, which is proportional to resistivity. This additional term changes the temperature dependence of ρ significantly, particularly when u_0 is itself substantial.

F. Pressure-dependent residual resistivity and magnetism

We now examine the effect of pressure on the magnetism and the electrical transport in the NiCoMn alloy. Figure 11(a) relates the lattice parameter to the "hydrostatic" pressure—defined as the average of the diagonal terms of the pressure tensor that is calculated using GGA. The pressure tensor is calculated using the supercell method based on a 108-atom SQS cell at various lattice parameters. All internal ionic degrees of freedom are optimized at each lattice parameter. A rough estimate gives 1 kbar hydrostatic compressive pressure, which reduces the lattice parameter by 0.83 m Å. The theoretical lattice parameter, corresponding to *zero* hydrostatic pressure, is 3.54 Å, which is 1.7% smaller than the experimental value.

The species-resolved magnetic moments in NiCoMn alloys are shown in Fig. 11(b). With reduced lattice parameters, the local moment on each species gradually decreases due

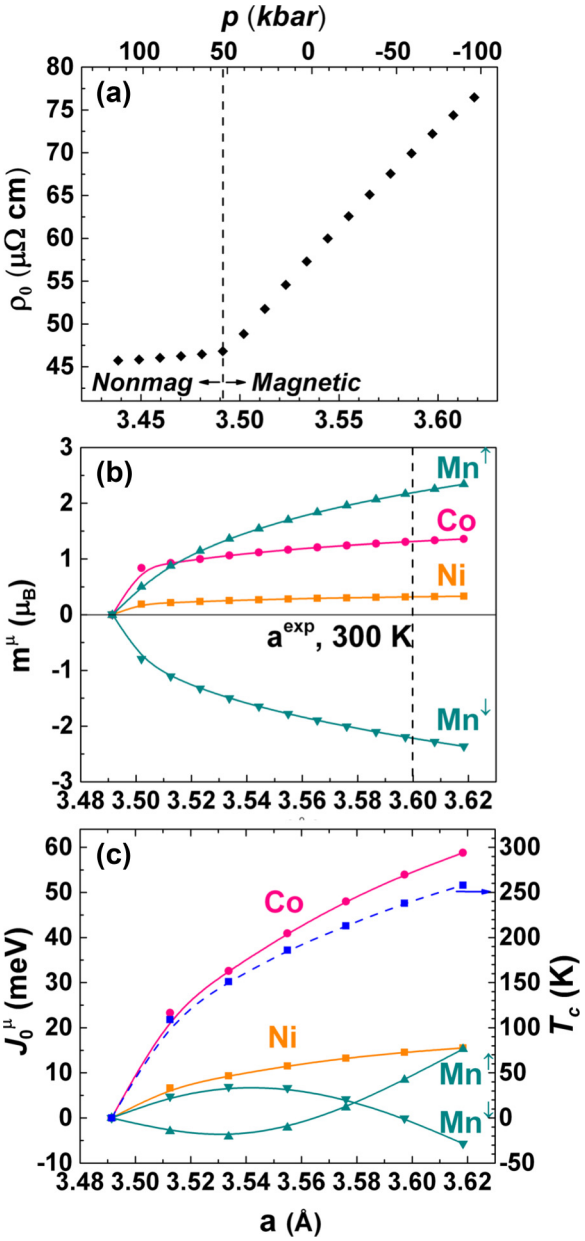

FIG. 11. (a) The residual resistivity (ρ_0, $\mu\Omega$ cm) at different lattice parameter. The hydrostatic pressures (P, kbar) at different lattice parameters are also labeled. (b) The lattice-parameter-dependent local moment on different species. The experimental lattice parameter is labeled using a dashed line. (c) Curie temperature (T_c, K) and effective exchange field on species μ (J_0^μ, meV) as a function of lattice parameter.

to the enhanced hybridization effect between 3d orbitals, and eventually no local moment is formed when the lattice parameter is smaller than 3.49 Å. It is worth noting that the local moments on $Mn^{\uparrow}$ and $Mn^{\downarrow}$ are more sensitive to the lattice parameter than the Ni or Co moments. This suggests that the enhanced electron hybridization is more pronounced for Mn 3d orbitals, thereby effectively reducing the density of states at the Fermi level and destroying the Mn local moments.

The effect of varying the lattice parameter on ρ_0 is shown in Fig. 11(a). With reduced local moments, ρ_0 decreases

drastically—at a rate of 2.4 $\mu\Omega$ cm per 0.01 Å—due to magnetic scattering. On the other hand, in the nonmagnetic phase—when $a \leqslant 3.49$ Å—ρ_0 becomes insensitive to the lattice parameter. With reduced lattice parameters in the nonmagnetic phase, the density of states at the Fermi level (carrier density) decreases while the band dispersion across the Fermi level (carrier mobility) increases as a result of the enhanced hybridization. The above two competing effects cancel each other out, making ρ_0 relatively insensitive to the lattice parameter. This result reveals the importance of the magnetism and its dependence on the lattice parameter or pressure on electron-mediated energy dissipation.

Figure 11(c) illustrates the effective exchange field on species μ (J_0^μ, meV) and the MC T_c as a function of lattice parameter. T_c mostly follows the more pronounced effective exchange field on Co (J_0^{Co}). Unlike J_0^{Ni}, J_0^{Co} is sensitive to the lattice parameter while the m^{Co} is relatively inert in a wide range of lattice parameters. We further confirm that the reduction of J_0^{Co} mainly comes from $J^{\mathrm{Co,Co}}$ within the first-nearest-neighbor shell. While both J_0^{Ni} and J_0^{Co} decrease with the lattice parameters, J_0^{Mn} exhibits nonmonotonic behavior, mainly from the complex nonmonotonic $J^{\mathrm{Mn,Mn}}$. The other $J^{\mathrm{Mn},\mu}$ ($\mu \neq$ Mn) reduces with the lattice parameter, as expected.

IV. CONCLUSIONS

By comparing with the electronic structure of the supercell method, the ground state of NiCoMn disordered solid solution alloys was verified and was denoted as the DLM-Mn state. The DLM-Mn state distinguishes two equally populated groups of Mn atoms, with large spin moments but opposite spin orientations. In contrast, the electronic structure of the AFM state, having only one type of Mn atom, is inconsistent with that from the supercell method.

Spin spiral calculations were performed for both the AFM and DLM-Mn states of disordered NiCoMn alloys, and we demonstrated the following:

(i) The AFM state is dynamically unstable in the sense that the energy reduces in the presence of spin noncollinearity, and an unphysical enhancement of Mn moments is also observed.

(ii) The DLM-Mn state is most energetically favorable in the spin spiral state, and no transparent longitudinal spin fluctuation is observed in the presence of spin noncollinearity in this state.

(iii) The applicability of the Heisenberg model is tested, providing a justification of thermodynamic study based on the Heisenberg model.

In addition, the exchange parameters were calculated using a linear-response expression, and the thermodynamics were simulated based on the Heisenberg model by using the classical mean-field approximation, the classical pair cluster approximation, and the classical Monte Carlo simulation. We found that the spin orientation on Mn easily becomes noncollinear/disordered at low temperatures ($T \ll T_c$). This is due to the relatively small Weiss field on Mn sites. We further demonstrated that a very low T_c is obtained when using exchange parameters from the (incorrect) AFM state. The magnetic transition temperature still requires experimental verification.

In the DLM-Mn ground state, the magnetic scattering is almost saturated at zero temperature due to the antiparallel spin alignments between Mn atoms. Full spin disorder beyond the T_C does not further contaminate the Fermi surface. We also demonstrate that even though the static displacements have a small effect on raising ρ_0, they can alter the temperature-dependent ρ strikingly when combined with the thermal displacements.

Finally, we found that a hydrostatic pressure of 50 kbar quenches the magnetism of NiCoMn, and that the resistivity is strongly correlated with the magnetism. This suggests a modest and positive contribution to the resistivity from thermal expansion.

ACKNOWLEDGMENTS

This work was supported as part of the Energy Dissipation to Defect Evolution (EDDE), an Energy Frontier Research Center funded by the U.S. Department of Energy, Office of Science, Basic Energy Sciences under Contract No. DE-AC05-00OR22725 (designed the research and performed all theoretical calculations). This research used resources of Oak Ridge National Laboratory's Compute and Data Environment for Science (CADES) and the Oak Ridge Leadership Computing Facility, which is a DOE Office of Science User Facility supported under Contract No. DE-AC05-00OR22725. S.W., S.M., and H.E. would like to thank the Deutsche Forschungsgemeinschaft for financial support within Priority Program SPP 1538 and the collaborative research centers 689 and 1277 (development of SPR-KKR program package). S.M. appreciates useful discussions with Hongbin Bei, Brian Sales, and Ke Jin.

This manuscript has been authored by UT-Battelle, LLC under Contract No. DE-AC05-00OR22725 with the U.S. Department of Energy. The U.S. Government retains and the publisher, by accepting the article for publication, acknowledges that the U.S. Government retains a nonexclusive, paid-up, irrevocable, worldwide license to publish or reproduce the published form of this manuscript, or allow others to do so, for U.S. Government purposes. The Department of Energy will provide public access to these results of federally sponsored research in accordance with the DOE Public Access Plan (http://energy.gov/downloads/doe-public-access-plan).

[1] J.-W. Yeh, S.-K. Chen, S.-J. Lin, J.-Y. Gan, T.-S. Chin, T.-T. Shun, C.-H. Tsau, and S.-Y. Chang, Nanostructured high-entropy alloys with multiple principal elements: Novel alloy design concepts and outcomes, Adv. Eng. Mater. **6**, 299 (2004).

[2] M.-H. Tsai and J.-W. Yeh, High-entropy alloys: A critical review, Mater. Res. Lett. **2**, 107 (2014).

[3] B. Cantor, I. T. H. Chang, P. Knight, and A. J. B. Vincent, Microstructural development in equiatomic multicomponent alloys, Mater. Sci. Eng. A **375–377**, 213 (2004).

[4] Z. Wu, H. Bei, F. Otto, G. M. Pharr, and E. P. George, Recovery, recrystallization, grain growth and phase stability of a family of FCC-structured multi-component equiatomic solid solution alloys, Intermetallics **46**, 131 (2014).

[5] B. Gludovatz, A. Hohenwarter, K. V. S. Thurston, H. Bei, Z. Wu, E. P. George, and R. O. Ritchie, Exceptional damage-tolerance of a medium-entropy alloy CrCoNi at cryogenic temperatures, Nat. Commun. **7**, 10602 (2016).

[6] B. Gludovatz, A. Hohenwarter, D. Catoor, E. H. Chang, E. P. George, and R. O. Ritchie, A fracture-resistant high-entropy alloy for cryogenic applications, Science **345**, 1153 (2014).

[7] Y. Zhang, G. M. Stocks, K. Jin, C. Lu, H. Bei, B. C. Sales, L. Wang, L. K. Béland, R. E. Stoller, G. D. Samolyuk *et al.*, Influence of chemical disorder on energy dissipation and defect evolution in concentrated solid solution alloys, Nat. Commun. **6**, 8736 (2015).

[8] C. Lu, L. Niu, N. Chen, K. Jin, T. Yang, P. Xiu, Y. Zhang, F. Gao, H. Bei, S. Shi *et al.*, Enhancing radiation tolerance by controlling defect mobility and migration pathways in multicomponent single-phase alloys, Nat. Commun. **7**, 13564 (2016).

[9] K. Jin, S. Mu, K. An, W. D. Porter, G. D. Samolyuk, G. M. Stocks, and H. Bei, Thermophysical properties of Ni-containing single-phase concentrated solid solution alloys, Mater. Des. **117**, 185 (2017).

[10] K. Jin, B. C. Sales, G. M. Stocks, G. D. Samolyuk, M. Daene, W. J. Weber, Y. Zhang, and H. Bei, Tailoring the physical properties of Ni-based single-phase equiatomic alloys by modifying the chemical complexity, Sci. Rep. **6**, 20159 (2016).

[11] B. C. Sales, K. Jin, H. Bei, G. M. Stocks, G. D. Samolyuk, A. F. May, and M. A. McGuire, Quantum critical behavior in a concentrated ternary solid solution, Sci. Rep. **6**, 26179 (2016).

[12] O. Schneeweiss, M. Friák, M. Dudová, D. Holec, M. Šob, D. Kriegner, V. Holý, P. Beran, E. P. George, J. Neugebauer *et al.*, Magnetic properties of the crmnfeconi high-entropy alloy, Phys. Rev. B **96**, 014437 (2017).

[13] O. N. Senkov, J. M. Scott, S. V. Senkova, D. B. Miracle, and C. F. Woodward, Microstructure and room temperature properties of a high-entropy TaNbHfZrTi alloy, J. Alloys Compd. **509**, 6043 (2011).

[14] M. Feuerbacher, M. Heidelmann, and C. Thomas, Hexagonal high-entropy alloys, Mater. Res. Lett. **3**, 1 (2015).

[15] A. Van De Walle and G. Ceder, The effect of lattice vibrations on substitutional alloy thermodynamics, Rev. Mod. Phys. **74**, 11 (2002).

[16] D. Ma, B. Grabowski, F. Körmann, J. Neugebauer, and D. Raabe, *Ab initio* thermodynamics of the CoCrFeMnNi high entropy alloy: Importance of entropy contributions beyond the configurational one, Acta Mater. **100**, 90 (2015).

[17] S. Zhao, G. M. Stocks, and Y. Zhang, Stacking fault energies of face-centered cubic concentrated solid solution alloys, Acta Mater. **134**, 334 (2017).

[18] C. Niu, C. R. LaRosa, J. Miao, M. J. Mills, and M. Ghazisaeidi, Magnetically-driven phase transformation strengthening in high entropy alloys, Nat. Commun. **9**, 1363 (2018).

[19] Z. Dong, S. Schönecker, W. Li, D. Chen, and L. Vitos, Thermal spin fluctuations in CoCrFeMnNi high entropy alloy, Sci. Rep. **8**, 12211 (2018).

[20] S. Mu, G. D. Samolyuk, S. Wimmer, M. C. Troparevsky, S. Khan, S. Mankovsky, H. Ebert, and G. M. Stocks, Uncovering electron scattering mechanisms in NiFeCoCrMn derived concentrated solid solution and high entropy alloys, npj Comput. Mater. **5**, 1 (2019).

[21] G. D. Samolyuk, S. Mu, A. F. May, B. C. Sales, S. Wimmer, S. Mankovsky, H. Ebert, and G. M. Stocks, Temperature dependent electronic transport in concentrated solid solutions of the 3*d*-transition metals Ni, Fe, Co and Cr from first principles, Phys. Rev. B **98**, 165141 (2018).

[22] M. van Schilfgaarde, I. A. Abrikosov, and B. Johansson, Origin of the invar effect in iron–nickel alloys, Nature (London) **400**, 46 (1999).

[23] T. Y. Chen, T. C. Chuang, S. Y. Huang, H. W. Yen, and C. F. Pai, Spin-Orbit Torque from a Magnetic Heterostructure of High-Entropy Alloy, Phys. Rev. Appl. **8**, 044005 (2017).

[24] Z. Wu, H. Bei, G. M. Pharr, and E. P. George, Temperature dependence of the mechanical properties of equiatomic solid solution alloys with face-centered cubic crystal structures, Acta Mater. **81**, 428 (2014).

[25] N. L. Okamoto, K. Yuge, K. Tanaka, H. Inui, and E. P. George, Atomic displacement in the CrMnFeCoNi high-entropy alloy—A scaling factor to predict solid solution strengthening, AIP Adv. **6**, 125008 (2016).

[26] A. Zunger, S.-H. Wei, L. G. Ferreira, and J. E. Bernard, Special Quasirandom Structures, Phys. Rev. Lett. **65**, 353 (1990).

[27] P. Soven, Coherent-potential model of substitutional disordered alloys, Phys. Rev. **156**, 809 (1967).

[28] S. Huang, W. Li, S. Lu, F. Tian, J. Shen, E. Holmström, and L. Vitos, Temperature dependent stacking fault energy of FeCrCoNiMn high entropy alloy, Scr. Mater. **108**, 44 (2015).

[29] S. Huang, E. Holmström, O. Eriksson, and L. Vitos, Mapping the magnetic transition temperatures for medium- and high-entropy alloys, Intermetallics **95**, 80 (2018).

[30] H. Akai and P. H. Dederichs, Local moment disorder in ferromagnetic alloys, Phys. Rev. B **47**, 8739 (1993).

[31] J. Korringa, On the calculation of the energy of a bloch wave in a metal, Physica **13**, 392 (1947).

[32] W. Kohn and N. Rostoker, Solution of the Schrödinger equation in periodic lattices with an application to metallic lithium, Phys. Rev. **94**, 1111 (1954).

[33] P. E. Blöchl, Projector augmented-wave method, Phys. Rev. B **50**, 17953 (1994).

[34] G. Kresse and J. Hafner, *Ab initio* molecular dynamics for open-shell transition metals, Phys. Rev. B **48**, 13115 (1993).

[35] G. Kresse and J. Furthmüller, Efficient iterative schemes for *ab initio* total-energy calculations using a plane-wave basis set, Phys. Rev. B **54**, 11169 (1996).

[36] H. J. Monkhorst and J. D. Pack, Special points for Brillouin-zone integrations, Phys. Rev. B **13**, 5188 (1976).

[37] J. P. Perdew, K. Burke, and M. Ernzerhof, Generalized Gradient Approximation Made Simple, Phys. Rev. Lett. **77**, 3865 (1996).

[38] H. Ebert *et al.*, The munich spr-kkr package, version 7.7, http://olymp.cup.uni-muenchen/de/ak/ebert/SPRKKR (2017).

[39] R. Kubo, Statistical-mechanical theory of irreversible processes. I. General theory and simple applications to magnetic and conduction problems, J. Phys. Soc. Jpn. **12**, 570 (1957).

[40] D. A. Greenwood, The Boltzmann equation in the theory of electrical conduction in metals, Proc. Phys. Soc. **71**, 585 (1958).

[41] W. H. Butler, Theory of electronic transport in random alloys: Korringa-Kohn-Rostoker coherent-potential approximation, Phys. Rev. B **31**, 3260 (1985).

[42] H. Ebert, S. Mankovsky, K. Chadova, S. Polesya, J. Minar, and D. Koedderitzsch, Calculating linear-response functions for finite temperatures on the basis of the alloy analogy model, Phys. Rev. B **91**, 165132 (2015).

[43] A. I. Liechtenstein, M. I. Katsnelson, V. P. Antropov, and V. A. Gubanov, Local spin density functional approach to the theory of exchange interactions in ferromagnetic metals and alloys, J. Magn. Magn. Mater. **67**, 65 (1987).

[44] R. Kikuchi, A theory of cooperative phenomena, Phys. Rev. **81**, 988 (1951).

[45] J. M. Sanchez, F. Ducastelle, and D. Gratias, Generalized cluster description of multicomponent systems, Physica A (Amsterdam) **128**, 334 (1984).

[46] V. G. Vaks and N. E. Zein, Theory of phase transitions in solid solutions, J. Exp. Theor. Phys. **40**, 537 (1975).

[47] V. G. Vaks and G. D. Samolyuk, On accuracy of different cluster models used in describing ordering phase transitions in fcc alloys, J. Exp. Theor. Phys. **88**, 89 (1999).

[48] R. H. Swendsen and J. S. Wang, Replica Monte Carlo Simulation of Spin-Glasses, Phys. Rev. Lett. **57**, 2607 (1986).

[49] K. Hukushima and K. Nemoto, Exchange Monte Carlo method and application to spin glass simulations, J. Phys. Soc. Jpn. **65**, 1604 (1996).

[50] U. Wolff, Collective Monte Carlo Updating for Spin Systems, Phys. Rev. Lett. **62**, 361 (1989).

[51] B. L. Gyorffy, A. J. Pindor, J. Staunton, G. M. Stocks, and H. Winter, A first-principles theory of ferromagnetic phase transitions in metals, J. Phys. F **15**, 1337 (1985).

[52] T. Fukushima, H. Katayama-Yoshida, K. Sato, M. Ogura, R. Zeller, and P. H. Dederichs, Local energies and energy fluctuations applied to the high entropy alloy CrFeCoNi, J. Phys. Soc. Jpn. **86**, 114704 (2017).

[53] L. M. Sandratskii, Energy band structure calculations for crystals with spiral magnetic structure, Phys. Status Solidi B **136**, 167 (1986).

[54] L. M. Sandratskii, Symmetry analysis of electronic states for crystals with spiral magnetic order. I. General properties, J. Phys.: Condens. Matter **3**, 8565 (1991).

[55] S. Mankovsky, G. H. Fecher, and H. Ebert, Electronic structure calculations in ordered and disordered solids with spiral magnetic order, Phys. Rev. B **83**, 144401 (2011).

[56] J. Kübler, *Theory of Itinerant Electron Magnetism* (Oxford University Press, Oxford, 2017), Vol. 106.

[57] S. V. Halilov, H. Eschrig, A. Y. Perlov, and P. M. Oppeneer, Adiabatic spin dynamics from spin-density-functional theory: Application to Fe, Co, and Ni, Phys. Rev. B **58**, 293 (1998).

[58] A. L. Wysocki, K. D. Belashchenko, J. P. Velev, and M. van Schilfgaarde, Calculations of spin-disorder resistivity from first principles, J. Appl. Phys. **101**, 09G506 (2007).